



HAL
open science

Long Slot Array Fed by a Nonuniform Corporate Feed Network in PPW Technology

Thomas Potelon, Mauro Ettorre, Ronan Sauleau

► **To cite this version:**

Thomas Potelon, Mauro Ettorre, Ronan Sauleau. Long Slot Array Fed by a Nonuniform Corporate Feed Network in PPW Technology. *IEEE Transactions on Antennas and Propagation*, 2019, 67 (8), pp.5436-5445. 10.1109/TAP.2019.2917581 . hal-02277953

HAL Id: hal-02277953

<https://univ-rennes.hal.science/hal-02277953>

Submitted on 11 Sep 2019

HAL is a multi-disciplinary open access archive for the deposit and dissemination of scientific research documents, whether they are published or not. The documents may come from teaching and research institutions in France or abroad, or from public or private research centers.

L'archive ouverte pluridisciplinaire **HAL**, est destinée au dépôt et à la diffusion de documents scientifiques de niveau recherche, publiés ou non, émanant des établissements d'enseignement et de recherche français ou étrangers, des laboratoires publics ou privés.

Long Slot Array Fed by a Non-Uniform Corporate Feed Network in PPW Technology

Thomas Potelon, Mauro Ettore, *Senior Member, IEEE*, and Ronan Sauleau, *Fellow, IEEE*.

Abstract—We present here a novel architecture of high-gain CTS (continuous transverse stub) antenna array operating at E-band (71-86GHz) with reduced side lobe level (SLL). The antenna consists of an array of 16 long slots excited by a non-uniform parallel-plate waveguide (PPW) corporate feed network. The non-uniform excitation is achieved by the design of asymmetrical power dividers in PPW technology, for which simple analytical models are provided. Full-wave simulations are validated by measurements of a prototype fabricated in aluminum. The SLL is lower than -28 dB in E-plane. Such a SLL is 15 dB lower than classical parallel-fed CTS arrays. The overall antenna SLL remains below -18 dB over the 75-86 GHz band. Its mean radiation efficiency is 60% and a maximum efficiency of 85% is reached at 86 GHz.

Index Terms— Broadband antenna, high-gain antenna, low-side lobe level antenna, millimeter-wave antenna, PPW technology, slot array, CTS antenna.

I. INTRODUCTION

The saturation of the frequency spectrum and the need for higher data rates has led to a migration of current data services (e.g. mobile networks, space communications, etc.) towards millimeter wave frequencies. However, at higher frequencies, the fabrication tolerances are more severe, and the material loss increases; therefore reaching high antenna efficiency becomes an issue. In particular, the feed networks of printed antennas, such as patch arrays or substrate integrated waveguide (SIW) antennas, are too dissipative to be considered for high gain applications at millimeter wave frequencies [1]. Similarly, dielectric lenses are often quite lossy above 30 GHz, e.g. [2]-[4].

To reach a good efficiency, purely hollow metallic solutions are preferred. Reflector antennas can easily achieve a high gain over a wide frequency band with a good efficiency; however their size makes them difficult to use in a discrete fashion [5]. Slotted rectangular waveguide antennas [6] are low-loss antennas but they may suffer from a dispersive behavior and their bandwidth might be limited [7]. Slotted cavity arrays fed by a corporate feed network in rectangular waveguide (RW) technology, combine both a high gain and a relatively broadband operation, up to 15% [8]-[10]. However, the various stages of the corporate networks are generally based on aperture coupling elements (e.g. slots). Such an element may limit the maximum frequency of operation due to fabrication constraints. Besides, corporate network in RW technology are very demanding in terms of fabrication accuracy. As an example, perfect electrical contact should be assured among the various

stage (with an immediate drawback in terms of cost and feasibility), although gap waveguides techniques allow to circumvent this issue [11].

In this context, continuous transverse stub (CTS) antennas are an attractive solution for high-gain wide-band applications [12]. They consist of an array of long slots fed by a parallel plate-waveguide (PPW) corporate feed network (CFN) operating with the non-dispersive transverse electric magnetic (TEM) mode. The true-time delay excitation combined with the TEM mode operation insure very broad band, theoretically wider than a decade [12], [13]. A long line current distribution is required for the excitation of such a structure. This is generally achieved by using a pillbox system [15] exciting the CFN. Such a feeding scheme preserves the low profile feature and wide band capability of the CTS array. In addition, beam steering capability can be achieved [16]. This combination of performance, unique to these antennas, makes them very appealing for various applications, e.g. [16]-[18].

However, to the authors' knowledge, all parallel-fed CTS antennas presented in the open literature use a uniform CFN based on symmetrical PPW T-junctions. This unavoidably leads to a side lobe level (SLL) of -13.5dB in E-plane, which is not acceptable for many telecommunication applications. We present here a novel parallel-fed CTS architecture providing, for the first time, reduced SLLs in the array plane (E-plane). This is achieved by imposing an illumination tapering over the slot array along this plane.

The paper is organized as follows. Section II discusses the design of the CFN according to the targeted power distribution over the array. This feed network is based on non-uniform PPW power dividers whose operation and design are presented in Section III. The overall antenna structure is detailed in Section IV. Section V describes the fabrication and assembly of the prototype and provides a successful comparison between full-wave results and measurements. Finally, conclusions are drawn in Section VI.

II. ANTENNA ARCHITECTURE AND PRE-DIMENSIONING

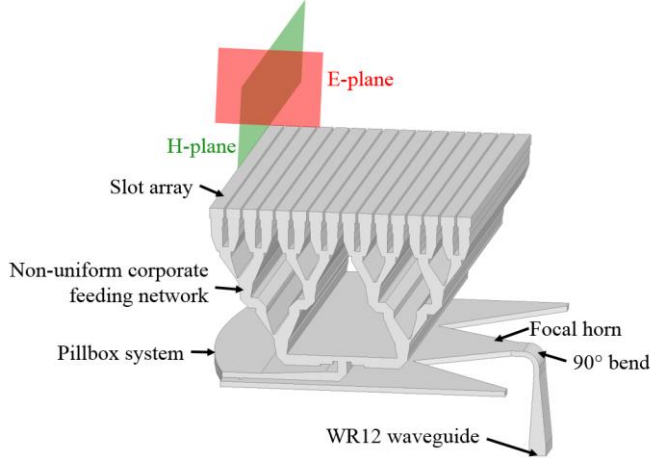


Fig. 1: 3D view of the antenna architecture.

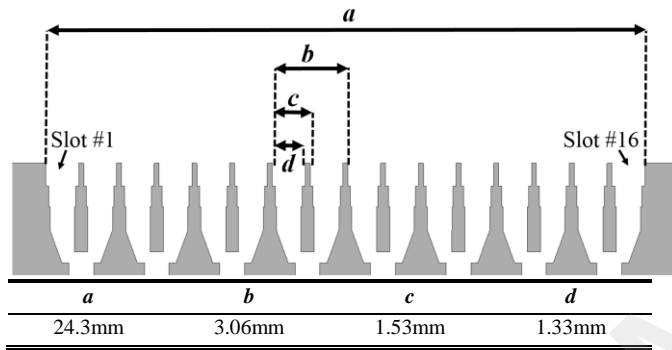


Fig. 2: Cross-section view of the slot array.

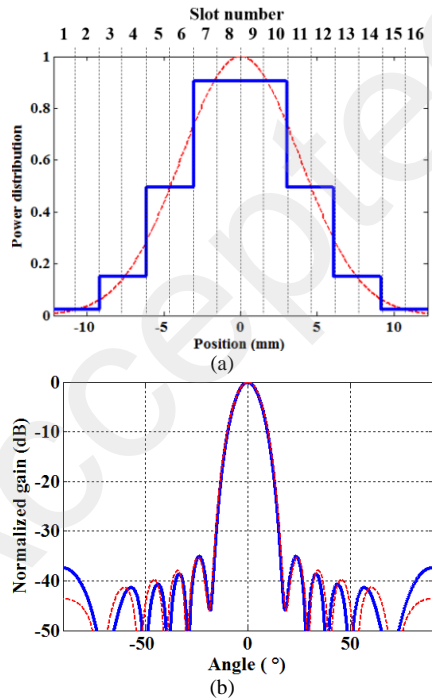


Fig. 3: (a) Power distributions over the array, and (b) corresponding radiation patterns at 78.5 GHz in E-plane for the ideal case (red dotted curve) and after discretization (blue solid curve).

Table 1: Division ratios of asymmetrical power dividers to achieve a SLL below -35 dB: comparison between the Gaussian and Taylor tapering.

Tapering technique	2 nd division stage	3 rd division stage (outer)	3 rd division stage (inner)
Gaussian	0.14	0.14	0.56
Taylor	0.13	0.11	0.59

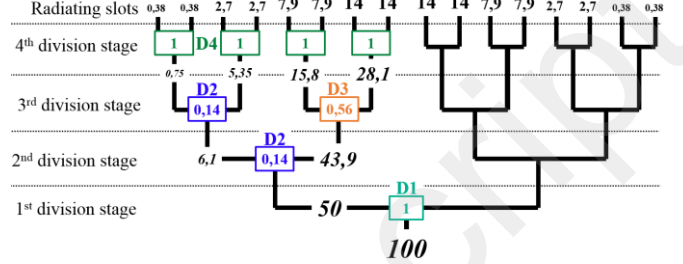


Fig. 4: Power division through the different branches of the corporate feed network (expressed in percentage of the input power). The division ratio is indicated for each power divider. A Gaussian tapering is assumed here (see Table 1).

A 3D view of the antenna architecture is represented in Fig. 1. The radiating part is a CTS array with 16 radiating slots. The CFN consists of PPW power dividers, with two outputs, distributed over four power division levels. The pillbox system is placed underneath and is excited by a standard WR12 waveguide. A right-angle bend is adopted to feed the antenna from the bottom. Apart from the WR12 waveguide and the focal horn, the whole antenna is designed with PPWs sized to support only the propagation of the TEM mode. The antenna is fabricated in aluminum to reduce losses.

The slot array is depicted in Fig. 2. The number of slots has been selected to reduce fabrication complexity while keeping a high gain. Note that the same concept and technology could be applied to much larger arrays, with 32 or 64 slots. The slot periodicity c is set to 0.4λ (where $\lambda=3.82$ mm is the wavelength in free space at 78.5 GHz), to avoid appearance of grating lobes. The total length a of the array equals 24.3mm (Fig. 2).

A Gaussian tapering of the power along the radiating aperture (Fig. 3a, dotted line) is adopted to reduce the SLL [19]. The selected power division is represented in Fig. 3a (solid line). An array factor approach was used to estimate the effect of the discretization of the power distribution over the aperture. The radiation patterns computed with these two power distributions are represented in Fig. 3b. This figure shows that the discretization has a marginal effect on the radiation pattern. Theoretically, the antenna should provide a full half-power beam-width (HPBW) of 11° and a SLL lower than -35 dB at 78.5 GHz.

The power division ratio of each power divider (i.e. the ratio between the two output powers) can be calculated from Fig. 3a. More precisely, Fig. 4 represents how the input power is distributed among the four division stages of the PPW feed network. The four dividers are labelled D_i ($i=1, \dots, 4$). The last division stage is made of equal power dividers D_4 , whose geometry is more compact than non-uniform power dividers, in order to be compatible with the slot array periodicity (see Fig. 2). The divider of the first division stage D_1 is also uniform to insure symmetry of the power distribution over the entire array, as plotted in Fig. 3a. The two central stages are composed of

non-uniform power dividers $D2$ and $D3$. The ratio of the power supported by each 2-slot sub-array to the total input power (presented in Fig. 4) is computed as the mean value of the perfect Gaussian distribution over the sub-array area (shown in Fig. 3(a)), normalized to the total radiated power. The division ratio of each power divider thus corresponds to the ratio of its output powers. Here, the desired power tapering (Fig. 3) yields to an identical division ratio (0.14) for the divider of the second stage and the outer divider of the third stage; as a result the same geometry is used ($D2$). Note that applying this design procedure to other array configurations may lead to different division ratios. In total, only two non-uniform power dividers, $D2$ and $D3$, are to be designed for the implementation of the non-uniform CFN. Their power division ratios are respectively 0.14 and 0.56. In this contribution a Gaussian tapering is adopted. However other solutions may be envisaged such as a classical Taylor tapering [20]. As an example, the comparison between a Gaussian and Taylor tapering in terms of division ratios to achieve a SLL of -35 dB is provided in Table 1.

The impact, on the overall radiation pattern, of discretizing the Gaussian function with the array of slots is described in Fig. 3b. This figure confirms that such a discretization has a limited effect on the radiation pattern. The main lobe is not affected at all. The high-order side lobes and nulls are slightly shifted but their levels are identical. A discrepancy between the ideal and discretized distribution is noticed around $\pm 90^\circ$. Nonetheless, the level of the side lobe is very low (below -36 dB). Exciting each radiating slot with an amplitude equal to the ideal Gaussian distribution would lead to a much more complex antenna architecture requiring asymmetrical power dividers in the last division stage. In such a case, apart from the side lobes around $\pm 90^\circ$ (below -36 dB), the other side lobe levels would not be significantly reduced. Moreover, applying the same approach to larger arrays (32 or 64 slots) would have an even more limited impact on the antenna radiation patterns.

III. ASYMMETRICAL POWER DIVIDERS IN PPW TECHNOLOGY

A. Geometry and operation

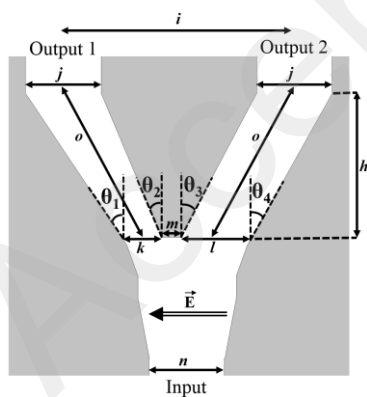


Fig. 5: Geometry (as seen in E-plane) and dimensions of the non-uniform power dividers $D2$ and $D3$.

	$D2$	$D3$
h	2.00mm	2.00mm
i	3.06mm	3.06mm
j	1.00mm	1.00mm
k	0.16mm	0.46mm
l	1.48mm	0.89mm
m	0.20mm	0.20mm
n	1.00mm	1.00mm
o	2.22mm	2.22mm
θ_1	36°	34°
θ_2	17°	22°
θ_3	32°	27°
θ_4	21°	30°

The geometry and dimensions of a non-uniform PPW power divider are defined in Fig. 5. Power division is realized by splitting the input PPW into two output PPWs of different heights k and l , the division ratio being theoretically equal to the ratio of the output PPW heights [21].

The thickness of the septum between the two output ports of the power divider (referred as m in Fig. 5) strongly affects its performance in terms of input matching. Therefore, such a thickness must be as small as possible. Here, for operation in E-band, it is set to the minimum thickness possible with the selected fabrication technology, namely 0.2 mm. The heights of the PPWs at the bifurcation level (k and l in Fig. 5) have been chosen to reduce losses and at the same time ease fabrication: large heights will reduce losses and are less sensible to potential fabrication errors. All angles (θ_1 to θ_4 in Fig. 5) are calculated to fulfill the following requirements

- The electrical path lengths between the input port and each output port are equal to insure uniform phase distribution among the radiating slots of the CTS array;
- The heights of the input (n) and output (j) PPWs are equal to facilitate their cascade in the CFN;
- The spacing i between the output PPWs equals 3.06 mm, which corresponds to twice the array slot periodicity, in order to easily fit in the 3rd division stage.

These requirements can be met easily using the equations reported in the appendix. The final dimensions obtained for $D2$ and $D3$ are given in Fig. 5.

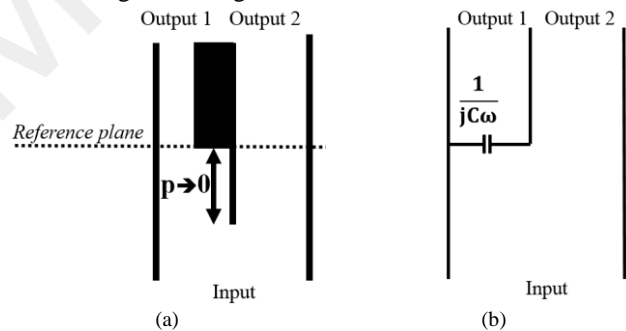


Fig. 6: (a) Geometry (depicted in E-plane) considered for the non-zero thickness septum bifurcation in E-plane with p tending towards 0, and (b) its equivalent lumped element circuit whose capacitance is provided in [21].

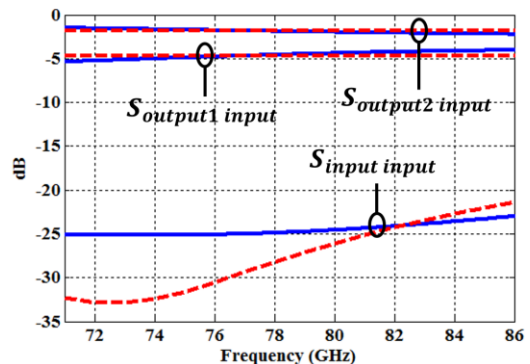


Fig. 7: Magnitude of the scattering parameters of power divider $D3$. Comparison between the circuit model results (blue solid curves) and full-wave simulations (red dash curve).

B. Lumped-element circuit model and performance

A simple circuit model was developed to ease the design procedure of the power divider. The structure is approximated by a cascade of several building blocks: linearly tapered lines, PPW bends and a bifurcation with a non-zero thickness septum. The two former geometries have already been analyzed in [21]. The bifurcation with a non-zero thickness septum has been studied in [22] and the authors provided an analysis applicable for any number of outputs. Here, the specific case of a two-output divider is used.

The bifurcation is seen as a cascade of a perfect junction (with a zero thickness septum) followed by a one-step reduction of one of the output PPW height, as illustrated in Fig. 6a. The equivalent circuits for both parts (perfect junction and PPW step reduction) can be found in [21], and the formula used to calculate the equivalent capacitance C is reported in Appendix. If the distance p between these parts tends towards 0, this model is equivalent to a non-zero thickness septum bifurcation. The resulting lumped element circuit can then be simplified to the one presented in Fig. 6b.

The scattering matrix of the non-uniform power divider is obtained by cascading the $ABCD$ matrix of each building block. The scattering parameters of power divider $D3$ computed using full-wave simulations [23] and the equivalent circuit model are represented in Fig. 7. We can observe a very good agreement between the two sets of results. The phase imbalance between both output ports (not represented here for the sake of brevity) is smaller than 10° ($\lambda/36$). Similar results have been obtained for $D2$. The difference in input reflection coefficients between the circuit model and full-wave simulations is attributed to uncounted reactive effects occurring at the transition between the input tapered line and the bifurcation septum. It is worth mentioning that such differences are in line with the error of the adopted circuit model in the order of 5% [21].

IV. ANTENNA DESIGN

In this section, the design and simulation results of the main building blocks are presented, as well as the simulated final antenna results. All simulations have been carried out using Ansys HFSS [23]. Metal losses are taken into account ($\sigma = 3.8 \times 10^7 \text{ S.m}^{-1}$ for aluminum blocks and $2 \times 10^6 \text{ S.m}^{-1}$ for steel).

A. CTS slot array and corporate feed network

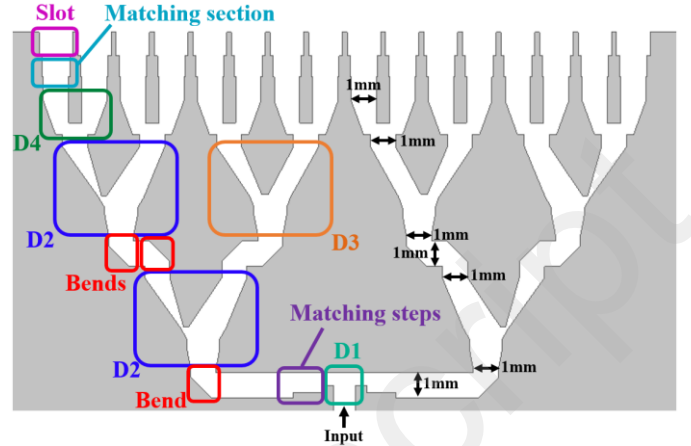


Fig. 8: Cross-section view in E-plane of the non-uniform corporate feed network (CFN) and its building blocks.

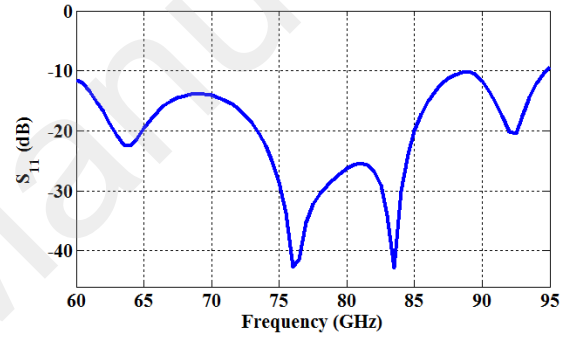


Fig. 9: Simulated input reflection coefficient of the CTS array fed by the non-uniform CFN.

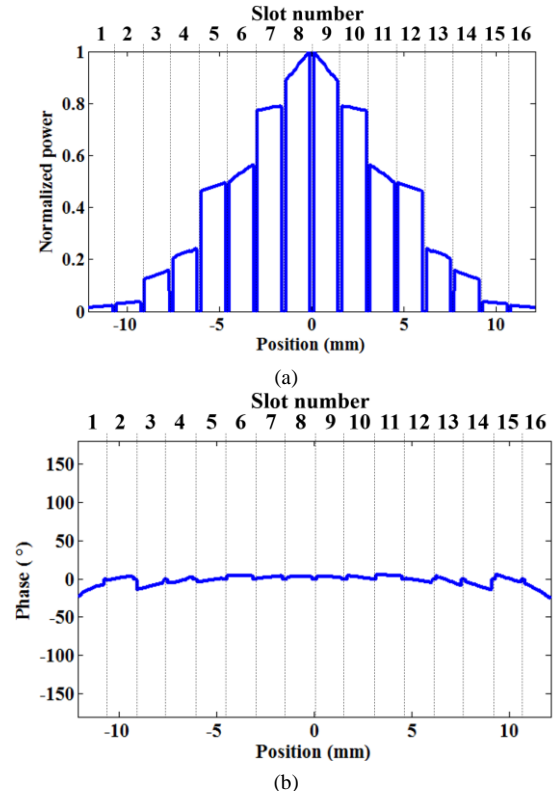


Fig. 10: Simulated power amplitude (a) and phase (b) distributions over the CTS array at 78.5 GHz.

The CTS array and its CFN are represented in Fig. 8 (cross-section view in E-plane). All the input and output PPWs of each building block have a height of 1mm (0.26λ at 78.5 GHz). The CFN was designed starting from the radiating slots to the input PPW of the antenna according to the procedure steps described below

- A two-step matching section is used below each radiating slot to match the active impedance of the array [13];
- A symmetrical geometry is used for the power dividers $D4$ due to space limitations;
- $D2$ and $D3$ dividers are placed right below the $D4$ junctions;
- Right angle bends are necessary to connect the two lower division stages. They are realized with a 45° chamfer;
- The first power divider $D1$ is a classical T-junction followed by two matching sections at each output. Two right angle bends are used for its connection to the other division stages.

The input reflection coefficient of the whole feed network (shown in Fig. 9) is lower than -15dB in E-band (71-86GHz) and does not exceed -10dB from 60 to 95GHz, corresponding to a 45% -10-dB bandwidth. The amplitude and phase distributions over the array are depicted in Fig. 10 at 78.5 GHz. The target amplitude distribution over the array is properly achieved. The maximum phase difference between the slots over the target frequency band (71-86GHz) is lower than 20° (corresponding to a physical path length difference of only 14 μm). This 20° phase error occurs at the extreme slots of the array with low radiating power, and therefore has no impact on the radiation patterns (see section IV.C).

B. Pillbox system

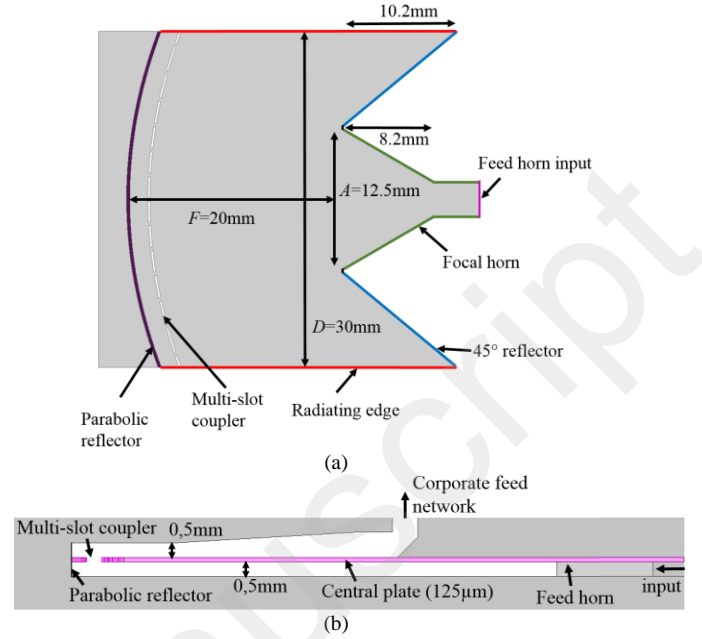


Fig. 11: Pillbox system: bottom view (a) and cut-view in E-plane (b).

A pillbox system (Fig. 11) has been selected to excite the CFN. Its fabrication with classical milling is very challenging since the two stacked PPWs (Fig. 11) consist of very thin hollow cavities, separated by a metal sheet containing the coupling slots [14], [16]. The major fabrication constraint is to keep a constant separation between both parallel plates over the large dimensions of the cavities. The central metallic plate, being very thin, can easily bend. It is worth mentioning that a dielectric spacer could be integrated in the structure. However, the goal here is to achieve a very efficient antenna solution and therefore additional dielectric losses were avoided. In the present case, the PPW heights are set to 0.5mm and the central plate thickness is $125\mu\text{m}$ to insure a good flatness (as depicted in Fig. 11b). Moreover the latter is fabricated in steel in order to improve its mechanical rigidity, at the expense of a reduced conductivity ($2 \times 10^6 \text{ S.m}^{-1}$) compared to Aluminum ($\sigma = 3.8 \times 10^7 \text{ S.m}^{-1}$).

The numerical tool presented in [17] was used to set the focal length F , the parabola diameter D and the focal horn aperture A in order to minimize the side lobe level in H-plane. The final geometrical dimensions are equal to 20 mm, 30 mm and 12.5 mm, respectively (Fig. 11). The procedure described in [14] is followed for the design of the quasi-optical system. The edge tapering of the pillbox system is lower than -15 dB in the overall band. Finally, 45° reflectors are placed on both sides of the focal horn to reduce spurious reflected power coming from the quasi-optical system. Such reflected power corresponds to less than 5% of the input power coming from the source. The residual power is then radiated in free space at the edges of the system, which are left open. Such a solution reduces the risk of possible interferences and resonances in the lower PPW and therefore leads to lower side lobes in H-plane. This solution is preferred to the integration of dummy ports or absorbing materials since it does not require any additional components and fabrication steps.

The input reflection coefficient for the simulated pillbox system is lower than -20 dB from 71 GHz to 86 GHz and remains below -10 dB from 64 GHz to 115 GHz (corresponding to a 57% fractional bandwidth). The SLL in H-plane of the radiated field remains below -24 dB over the same bandwidth. This low SLL value originates from the low edge illumination level of the parabola (-15 dB).

C. Overall antenna simulation results

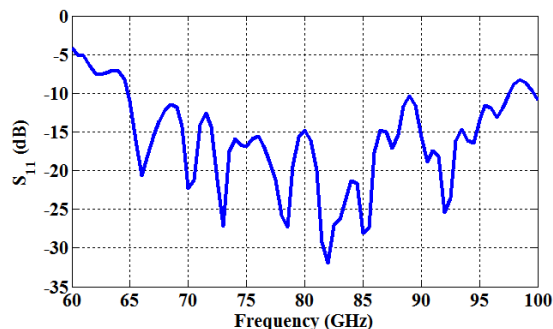


Fig. 12: Simulated input reflection coefficient of the entire antenna module.

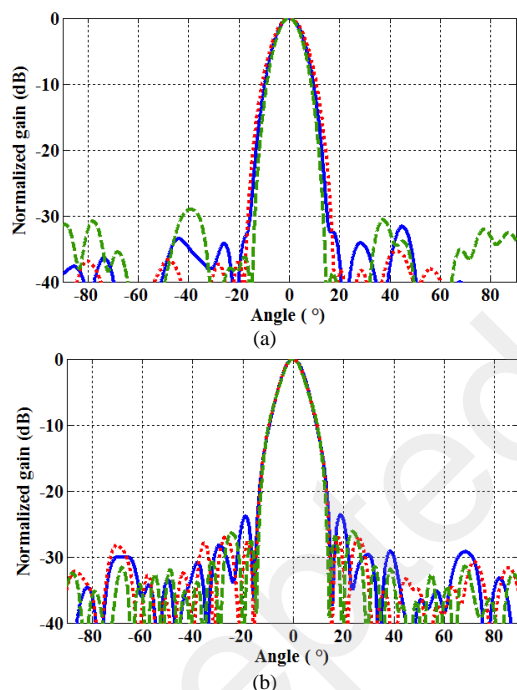


Fig. 13: Simulated radiation patterns in E-plane (a) and H-plane (b) at 71 GHz (red dotted curves), 78.5 GHz (blue solid curves) and 86 GHz (green dash curves).

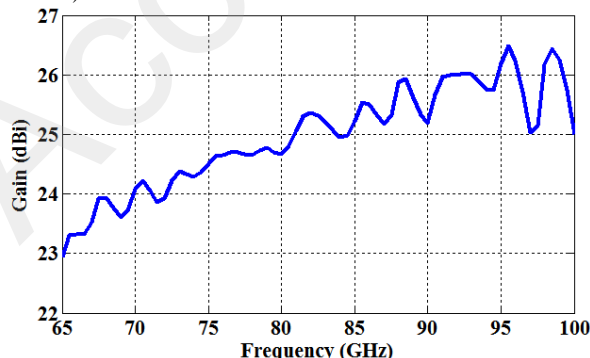


Fig. 14: Simulated gain of the overall antenna system.

The overall antenna system was simulated with Ansys HFSS [23].

The input reflection coefficient is depicted in Fig. 12. The antenna is matched below -12 dB over the full E-band (71-86 GHz) and below -10 dB from 65 to 97 GHz (40% fractional bandwidth). The radiation patterns in E- and H-planes are shown in Fig. 13 (a) and (b) at central and extreme frequencies of the target band. In E-plane, thanks to the non-uniform CFN, the SLL is lower than -29 dB over the whole frequency band. The SLL remains below -23 dB in H-plane due to the chosen edge tapering of the pillbox transition. The simulated gain, plotted in Fig. 14, varying between 24.0 dBi and 25.6 dBi over the 71-86 GHz band and from 23.0 dBi to 26.4 dBi between 65 and 100 GHz.

V. FABRICATION AND EXPERIMENTAL RESULTS

A. Fabrication techniques

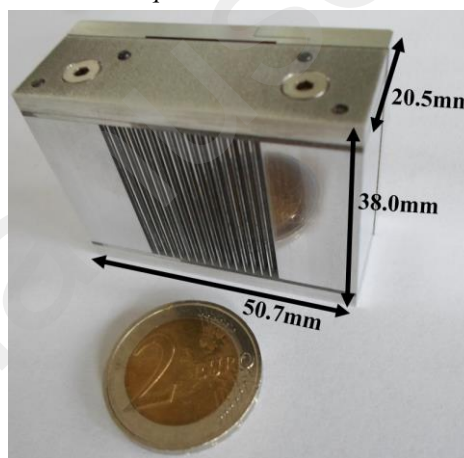
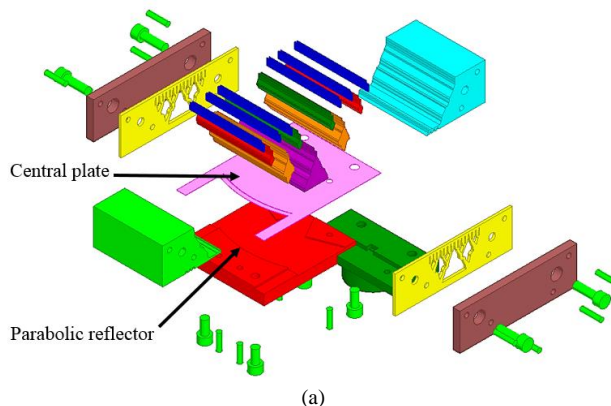


Fig. 15: 3D view of the fabricated prototype.



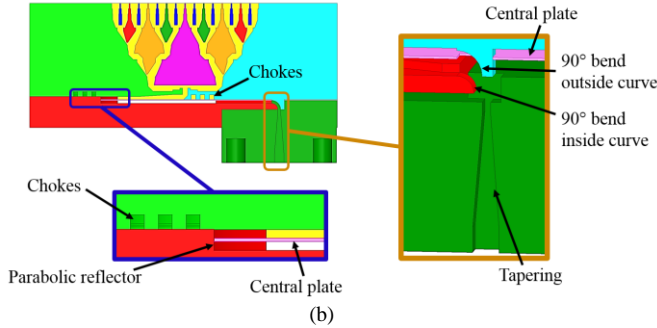


Fig. 16: Exploded view (a) and cross-sectional-view (b) of the antenna assembly.

The antenna was fabricated in metal using milling and electro-erosion techniques. All pieces were made in aluminum ($3.8 \times 10^7 \text{ S.m}^{-1}$) except the pillbox central plate which is in steel ($2 \times 10^6 \text{ S.m}^{-1}$) for a better mechanical stability. The fabrication accuracy is about $10 \mu\text{m}$. Only screws and dowels are used for assembly. The final size of the prototype is $50.7 \times 38 \times 20.5 \text{ mm}^3$ as shown in Fig. 15.

The assembly technique of the radiating slots and the corporate feed network is similar to the one proposed in [16] and [17]. An exploded view of the procedure is shown in Fig. 16. The minimum PPW height throughout the CFN is 0.125 mm , which can be easily realized using this fabrication and assembly procedure.

To avoid discontinuity and thus losses for the TEM mode supported by the pillbox system, the parabolic reflector was realized in a single aluminum block. The metallic plate with the coupling slot was then shaped as shown in Fig. 16a. Quarter-wavelength chokes were also used to improve the electrical contact between the different aluminum blocks (see Fig. 16b).

The selected antenna assembly only requires simple aluminum blocks to be manufactured and guarantees a good mechanical robustness as well as reduced metallic losses.

B. Experimental results

The fabricated prototype has been characterized at IETR using a compact antenna test range operating with a WR10 interface. A waveguide transition WR12 to WR10 was used for measurements. Therefore, due to the WR10 interface, the measurements are not calibrated below 75 GHz , and they are only presented for the $75\text{-}86 \text{ GHz}$ band.

The measured radiation patterns are compared to the simulated ones in E-plane (Fig. 17a-c) and H-plane (Fig. 17d-f). In E-plane, a very good agreement is observed between measurements and simulations: the main lobes match perfectly and the SLL is lower than -28 dB over the full band. This level is more than 15 dB lower than previously presented parallel-fed CTS antennas [16]-[18]. The comparison between the measured pattern and the one expected from the perfect Gaussian repartition (see Section II) is provided in Fig. 18. A very good agreement is observed again for the main lobe. The SLL is lower than -30 dB . These results validate the design of the non-uniform CFN architecture and the reliability of the employed fabrication techniques. In H-plane, a good agreement is obtained for the main lobe, even though the SLL is higher than expected. However, it still remains below -18 dB from 75 to 86 GHz . Specific simulations confirmed that the difference in SLL along the H-plane is caused by an $80\text{-}\mu\text{m}$ misalignment between the pillbox central plate (depicted in Fig. 11b and Fig. 16b) and the parabolic reflector. This creates an unexpected long coupling slot connecting the two PPWs along the parabolic reflector, affecting the operation of the multi-slot coupler. The overall antenna SLL remains lower than -18 dB in any plane from 75 to 86 GHz .

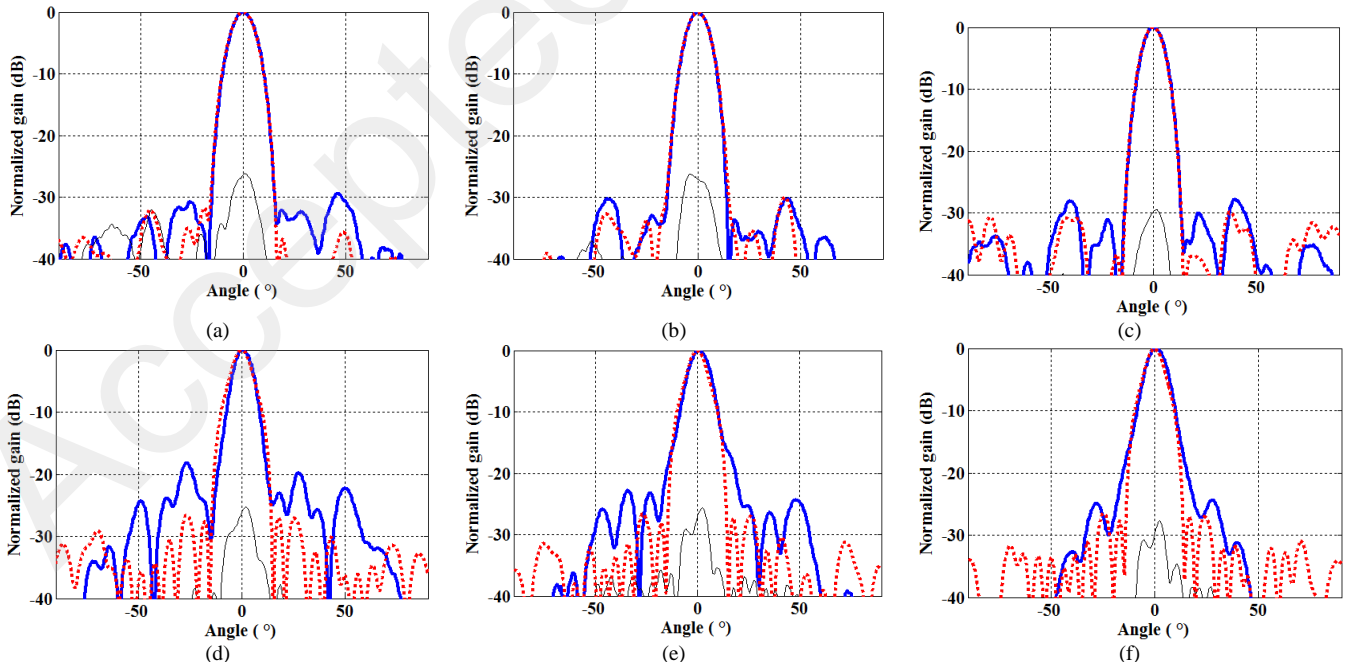


Fig. 17: Radiation patterns in E-plane at 75 GHz (a), 81 GHz (b) and 86 GHz (c), and in H-plane at 75 GHz (d), 81 GHz (e) and 86 GHz (f); measurement results (blue solid curves), simulation results (dotted red curves) and measured cross-polarization (thin grey curves).

The measured input reflection coefficient is reported in Fig. 19. It remains below -10 dB between 76 GHz and 86 GHz. The higher input reflections as compared to the simulated results are mainly caused by the previously mentioned 80- μm shift of the pillbox central plate and a misalignment (in the order of 70 μm) between the pieces composing the input 90° bend. This is confirmed by Fig. 20.b where a good agreement is observed between measured gain and simulated gain accounting for the misalignments (green dash curve). This assumption is strengthened by the excellent agreement between the simulated and measured radiation patterns in E-plane, ensuring that no significant mismatch occurs in the CFN and CTS array.

The measured directivity and gain are provided in Fig. 20a and Fig. 20b, respectively. Once again, only the results are provided in W-band since the measurement setup is considered calibrated above 75 GHz. The measured results are in good agreement with simulations, with an average difference between the measured and simulated directivity of 0.5 dB. The measured gain shows additional losses with respect to the simulated one, as reported in Fig. 20b. The additional losses are mainly caused by the 80- μm shift between the pillbox central plate and the reflector and a 70- μm misalignment at the input 90° bend level. More specifically, Fig. 20.b shows the computed gain considering misalignments at the pillbox reflector and the input bend (green dash curve). In this case, a good agreement can be observed between the measured and simulated gains. The remaining losses (less than 1 dB in average) are attributed to additional metallic losses caused by the surface roughness (not considered in the simulations). The overall antenna radiation efficiency is plotted in Fig. 21. It varies between 25% and 85%, with a mean efficiency of 60%. The radiation efficiency reduction at lower frequencies is caused by misalignments occurring at the pillbox coupler and input bend levels. Nevertheless, these results are above the state-of-the-art for parallel-fed CTS antennas operating above 60 GHz [17], [18]. Note that the measured E-plane radiation patterns (exclusively shaped by the non-uniform CFN and the CTS array) are in excellent agreement with simulations (Fig. 17). On the other hand, the measured H-plane patterns (exclusively shaped by the pillbox system) slightly differ from the simulated results (Fig. 17). This is caused by the 80- μm shift between the pillbox central plate and the reflector. We can conclude that the proposed non-uniform CFN and CTS array are perfectly functioning and do not contribute significantly to the antenna efficiency reduction.

The power budget defined at the design central frequency (78.5 GHz) is provided in Table 2.

The misalignments at the reflector and input 90° bend levels could be relaxed by feeding the antenna from the side instead of from the back as done here (this choice was made to ease its experimental characterization in anechoic chamber).

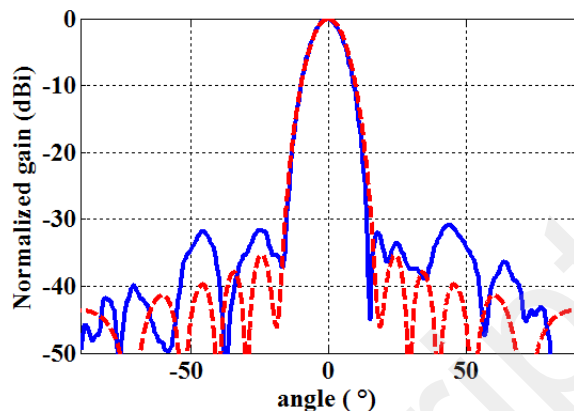


Fig. 18: Radiation patterns in E-plane at 78.5GHz: measured results (blue solid curve) and theoretical results from a non-discretized Gaussian distribution (red dotted curve, Fig. 3b).

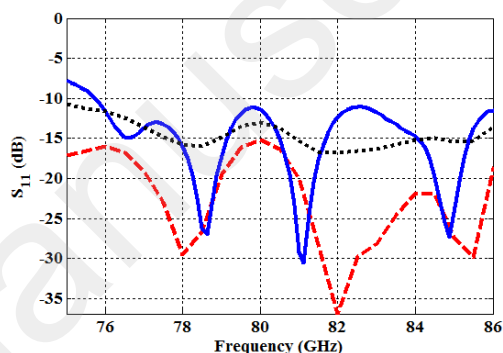


Fig. 19: Input reflection coefficients: comparison between the measured results (blue solid curves), the simulated results with perfect assembly (red dash curves) and with a 80- μm misalignment between the central plate and the parabolic reflector (black dotted curve).

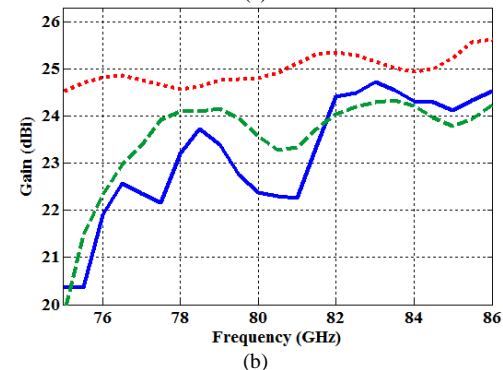
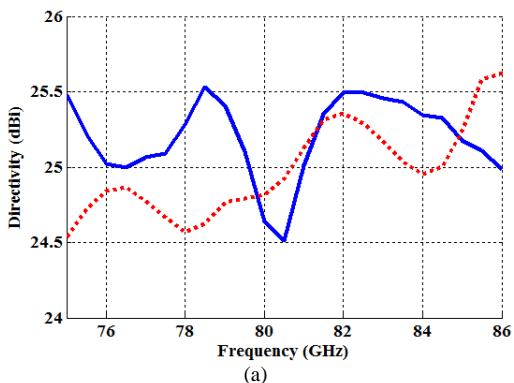


Fig. 20: (a) Comparison between the simulated (red dotted curve) and measured (blue solid curve) directivity; and gain (b) comparison between the simulated gain for ideal mechanical assembly (red dotted curve),

simulated gain with misalignments at the 90° input bend and pillbox levels (green dash curve) and measured gain (blue solid curve).

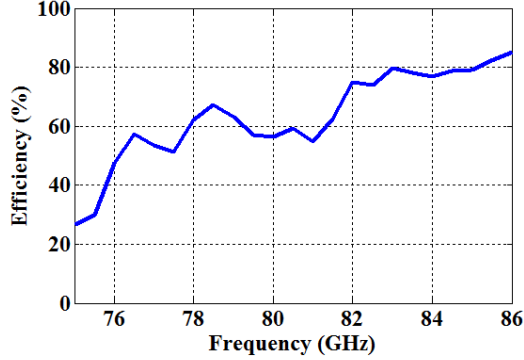


Fig. 21: Measured efficiency of the entire antenna system calculated from the experimental directivity and gain.

Table 2: Overall antenna power budget at 78.5GHz.

Measured directivity	25.4 dBi
Estimated metallic losses	0.5 dB
Estimated reflection loss at the reflector level	0.3 dB
Estimated leakage at the input bend level	0.5 dB
Calculated gain	24.1 dBi
Measured gain	23.9 dBi

VI. CONCLUSION

An innovative CTS array of long slots fed by a quasi-optical system is proposed at E-band. For the first time, a novel non-uniform corporate feeding network is used to illuminate the array of slots. The SLL is then controlled in E-plane, while the SLL level in H-plane is tuned by selecting properly the edge tapering of the pillbox transition. The corporate feed network relies on a new geometry of non-uniform power dividers in PPW technology, for which a lumped-element circuit model has been provided and successfully validated by full-wave simulations. An elaborated assembly was employed to ease the antenna fabrication using milling and electro-erosion of metal pieces. In simulation, the antenna performance is excellent: it covers a frequency band from 71 to 86 GHz with a gain greater than 24 dBi and side lobes lower than -29 dB in E-plane and -23 dB in H-plane. Moreover, the antenna could cover a broader band since it is matched below -10 dB from 65 to 97 GHz (40% fractional bandwidth). Measurements of a fabricated prototype confirm the numerical results. In E-plane the SLL is lower than -28 dB over the target frequency band (71-86 GHz). The antenna SLL remains below -18 dB in H-plane in the entire E-band. The gain is fairly constant from 76 GHz to 86 GHz with a maximum of 24.6 dBi. Using other assembly procedures or metal-only fabrication technologies (additive technologies, diffusion bonding) in order to avoid the misalignments and air gaps at the input bend and pillbox coupler levels could further result in a substantial overall antenna efficiency improvement.

This antenna proposes a unique combination of a low profile, a high gain, a broad bandwidth and a reduced SLL, which could be further combined with a beam scanning capability. This solution offers a low-profile alternative to reflector and lens antennas for high gain applications such as next generation mobile cellular networks. Applying this technique to larger

arrays becomes even more advantageous. As an example, adding two non-uniform division stages in order to excite a 64-slot array would increase the total antenna height by only 11mm (since each non-uniform division stage used in the proposed antenna design has a total height of 5.5mm). The antenna total height would then be about 32mm, and the 64-slot array would be almost 100mm long. A lens- or reflector-based antenna with the same profile would have an F/D ratio (focal distance over lens/reflector diameter) of 0.32, whereas typical values of F/D ratios are in the order of 0.8 for lens/reflector antennas, clearly showing the advantages of the proposed structure [24].

APPENDIX

The PPW angles for the non-uniform power divider outputs (represented in Fig. 5) can be obtained using the following formulas

$$\tan(\theta_1) = \frac{i + j - \frac{3k}{2} - \frac{l}{2} - m}{2h} \quad (A1)$$

$$\tan(\theta_2) = \frac{i - j + \frac{k}{2} - \frac{l}{2} - m}{2h} \quad (A2)$$

$$\tan(\theta_3) = \frac{i - j - \frac{k}{2} + \frac{l}{2} - m}{2h} \quad (A3)$$

$$\tan(\theta_4) = \frac{i + j - \frac{k}{2} - \frac{3l}{2} - m}{2h} \quad (A4)$$

The capacitance C of Fig. 6 can be calculated as follows (for the complete calculation, refer to [21])

$$C \approx \frac{2(k+m)}{\lambda} \left(\ln \left(\frac{1-\alpha^2}{4\alpha} \right) \left(\frac{1+\alpha}{1-\alpha} \right)^{1/2(\alpha+\frac{1}{\alpha})} \right) + \frac{2}{A} \quad (A5)$$

$$\alpha = \frac{k}{m} \quad (A6)$$

$$A = \left(\frac{1+\alpha}{1-\alpha} \right)^{2\alpha} \frac{1 + \sqrt{1 - \left(\frac{k+m}{\lambda} \right)^2}}{1 - \sqrt{1 - \left(\frac{k+m}{\lambda} \right)^2}} - \frac{1+3\alpha^2}{1-\alpha^2} \quad (A7)$$

ACKNOWLEDGMENT

This work is partly supported by the European Union through the European Regional Development Fund (ERDF), and also by Ministry of Higher Education and Research, Brittany and Rennes Métropole, through the CPER Project SOPHIE/STIC & Ondes.

REFERENCES

- [1] E. Levine, G. Malamud, S. Shtrikman, and D. Treves, "A study of microstrip array antennas with feed network," *IEEE Trans. Antennas Propag.*, vol. 37, no. 4, pp. 426-464, Apr. 1989.
- [2] B. Schoenlinner, X. Wu, J. P. Ebling, G. V. Eleftheriades, and G. M. Rebeiz, "Wide-angle spherical-lens antennas for automotive radars," *IEEE Trans. Antennas Propag.*, vol. 50, no. 9, pp. 2166-2175, Nov. 2002.
- [3] B. Barès and R. Sauleau, "Electrically-small shaped integrated lens antennas: a study of feasibility in Q-band," *IEEE Trans. Antennas Propag.*, vol. 55, no. 4, pp. 1038-1044, Apr. 2007.
- [4] J. R. Costa, C. A. Fernandes, G. Godi, R. Sauleau, L. Le Coq, and H. Legay, "Compact Ka-band lens antennas for LEO satellites," *IEEE Trans. Antennas Propag.*, vol. 56, no. 5, pp. 1251-1258, May 2008.
- [5] P. Zheng, G. Q. Zhao, S. H. Xu, F. Yang, and H. J. Sun, "Design of a W-band full-polarization monopulse cassegrain antenna," *IEEE Antennas Wireless Propag. Lett.*, vol. 16, Apr. 2016.
- [6] M. Zhang, J. Hirokawa, and M. Ando, "A four-corner-fed double-layer waveguide slot array with low sidelobes developed for a 40 GHz-band DDD system," *IEEE Trans. Antennas Propag.*, vol. 64, no. 59, pp. 2005-2010, Mar. 2016.
- [7] M. Ando, Y. Tsunemitsu, Z. Miao, and J. Hirokawa, "Reduction of long line effects in single-layer slotted waveguide arrays with an embedded partially corporate feed," *IEEE Trans. Antennas Propag.*, vol. 58, no. 7, pp. 2275-2280, Mar 2010.
- [8] Y. Miura, J. Hirokawa, M. Ando, Y. Shibuya, and G. Yoshida, "Double-layer full-corporate-feed hollow-waveguide slot array antenna in the 60-GHz band," *IEEE Trans. Antennas Propag.*, vol. 59, no. 8, pp. 2844-2851, Jun. 2011.
- [9] D. Zarifi, A. Farahbakhsh, A. U. Zaman, and P. S. Kildal, "Design and fabrication of a high-gain 60-GHz corrugated slot antenna array with ridge gap waveguide distribution layer," *IEEE Trans. Antennas Propag.*, vol. 64, no. 7, pp. 2905-2913, May. 2016.
- [10] K. Tekkouk, J. Hirokawa, K. Oogimoto, T. Nagatsuma, H. Seto, Y. Inoue, and M. Saito, "Corporate-feed slotted waveguide array antenna in the 350-GHz band by silicon process," *IEEE Trans. Antennas Propag.*, vol. 65, no. 1, pp. 217-225, Nov. 2017.
- [11] A. U. Zaman and P. S. Kildal, "Wide-band slot antenna arrays with single-layer corporate-feed-network in ridge gap waveguide technology," *IEEE Trans. Antennas Propag.*, vol. 62, no. 6, pp. 2992-3001, Jun. 2014.
- [12] W. W. Milroy, "Compact, ultrawide-band antenna feed architecture comprising a multistage, multilevel network of constant reflection-coefficient components," U.S. Patent 6 075 494, Jun. 2000.
- [13] F. Foglia Manzillo, M. Ettore, M. Casaletti, N. Capet, and R. Sauleau, "Active impedance of infinite parallel-fed continuous transverse stub array," *IEEE Trans. Antennas Propag.*, vol. 63, no. 7, pp. 3291-3297, Apr. 2015.
- [14] M. Ettore, R. Sauleau, and L. Le Coq, "Multi-beam multi-layer leaky-wave SIW pillbox antenna for millimeter-wave applications," *IEEE Trans. Antennas Propag.*, vol. 59, no. 4, pp. 1093-1100, Apr. 2011.
- [15] W. Rotman, "Wide-angle scanning with microwave double-layer pillboxes," *IRE Trans. Antennas Propag.*, vol. 6, no. 1, pp. 96-105, Jan. 1958.
- [16] M. Ettore, F. Foglia Manzillo, M. Casaletti, R. Sauleau, L. Le Coq, and N. Capet, "Continuous transverse stub array for Ka-band applications," *IEEE Trans. Antennas Propag.*, vol. 63, no. 9, pp. 4798-4800, Sep. 2015.
- [17] T. Potelon, M. Ettore, L. Le Coq, T. Bateman, J. Francey, D. Lelaidier, E. Seguenot, F. Devillers, and R. Sauleau, "A low-profile broadband 32-slot continuous transverse stub array for backhaul applications in E-band," *IEEE Trans. Antennas Propag.*, vol. 65, no. 12, pp. 6307-6316, Dec. 2015.
- [18] F. Foglia Manzillo, M. Ettore, M. S. Lathi, K. T. Kautio, D. Lelaidier, E. Seguenot, and R. Sauleau, "A multilayer LTCC solution for integrating 5G access point antenna modules," *IEEE Trans. Microwave Theory Tech.*, vol. 64, no. 7, pp. 2272-2283, Jul. 2016.
- [19] A. W. Rudge, K. Milne, A. D. Olver, and P. Knight, "The handbook of antenna design," *IEE Electromagnetic Waves Series 15*, vol.1, Peter Peregrinus Ltd., 1982.
- [20] T. T. Taylor, "One parameter family of line sources producing modified $\sin(\pi u)/\pi u$ patterns," *Hughes Aircraft Co. Tech. Mem. 324*, Culver City, USA, Sep. 1953.
- [21] N. Marcuvitz, "Waveguide handbook," Dover Publications Inc., 1965.
- [22] R. R. Mansour and R. H. Macphie, "Scattering at an N-furcated parallel-plate waveguide junction," *IEEE Trans. Microwave Theory Tech.*, vol. 33, no. 9, pp. 830-835, Sep. 1985.
- [23] HFSS, version 2018.2, ANSYS, Inc. Southpointe, 2600 ANSYS Drive, Cononsburg, PA 15317, USA.
- [24] C. A. Balans, "Antenna theory: analysis and design," Wiley Inc., 2005.